



HAL
open science

Single-cell data reveal heterogeneity of investment in ribosomes across a bacterial population

Antrea Pavlou, Eugenio Cinquemani, Corinne Pinel, Nils Giordano, Mathilde Van Melle-Gateau, Irina Mihalcescu, Johannes Geiselman, Hidde de Jong

► **To cite this version:**

Antrea Pavlou, Eugenio Cinquemani, Corinne Pinel, Nils Giordano, Mathilde Van Melle-Gateau, et al.. Single-cell data reveal heterogeneity of investment in ribosomes across a bacterial population. Nature Communications, 2025, 16 (1), pp.285. 10.1038/s41467-024-55394-5 . hal-04880507

HAL Id: hal-04880507

<https://inria.hal.science/hal-04880507v1>

Submitted on 10 Jan 2025

HAL is a multi-disciplinary open access archive for the deposit and dissemination of scientific research documents, whether they are published or not. The documents may come from teaching and research institutions in France or abroad, or from public or private research centers.

L'archive ouverte pluridisciplinaire **HAL**, est destinée au dépôt et à la diffusion de documents scientifiques de niveau recherche, publiés ou non, émanant des établissements d'enseignement et de recherche français ou étrangers, des laboratoires publics ou privés.



Distributed under a Creative Commons Attribution - NonCommercial - NoDerivatives 4.0 International License








Single-cell data reveal heterogeneity of investment in ribosomes across a bacterial population

Received: 10 April 2024

Accepted: 10 December 2024

Published online: 02 January 2025

 Check for updates

Antrea Pavlou^{1,2}, Eugenio Cinquemani ^{1,2}, Corinne Pinel^{1,2}, Nils Giordano ³,
Van Melle-Gateau Mathilde², Irina Mihalcescu ²,
Johannes Geiselmann ^{1,2,4}  & Hidde de Jong ^{1,2,4} 

Ribosomes are responsible for the synthesis of proteins, the major component of cellular biomass. Classical experiments have established a linear relationship between the fraction of resources invested in ribosomal proteins and the rate of balanced growth of a microbial population. Very little is known, however, about how the investment in ribosomes varies over individual cells in a population. We therefore extended the study of ribosomal resource allocation from populations to single cells, using a combination of time-lapse fluorescence microscopy and statistical inference. We found a large variability of ribosome concentrations and growth rates in conditions of balanced growth of the model bacterium *Escherichia coli* in a given medium, which cannot be accounted for by the population-level growth law. A large variability in the allocation of resources to ribosomes was also found during the transition of the bacteria from a poor to a rich growth medium. While some cells immediately adapt their ribosome synthesis rate to the new environment, others do so only gradually. Our results thus reveal a range of strategies for investing resources in the molecular machines at the heart of cellular self-replication. This raises the fundamental question whether the observed variability is an intrinsic consequence of the stochastic nature of the underlying biochemical processes or whether it improves the fitness of *Escherichia coli* in its natural environment.

Microbial growth involves the conversion of nutrients from the environment into biomass. The main component of biomass are proteins, which also play a major role in the synthesis of new biomass by functioning as enzymes in metabolism and by constituting the molecular machinery responsible for the synthesis of proteins and other macromolecules. Microbial growth therefore requires the coordinated investment of cellular resources in different categories of proteins. The basic principles of this coordination have been described by so-called growth laws^{1–3}. Growth laws relate the growth rate of the cells to

the abundance of different categories of proteins. In other words, they quantitatively describe the resource allocation strategies adopted by microbial cells.

A classical growth law states that there exists a linear relationship between growth rate and the mass fraction or concentration of ribosomal proteins^{4–11}. Ribosomes are probably the most important protein category for two reasons. First, they are responsible for the synthesis of all proteins in the cell. Second, they are themselves very costly to make: ribosomes constitute up to 40–50% of the total protein

¹Univ. Grenoble Alpes, Inria, Grenoble, France. ²Univ. Grenoble Alpes, CNRS, LIPhy, Grenoble, France. ³Nantes Université, INSERM, CNRS, Université d'Angers, CRI2NA, Nantes, France. ⁴These authors contributed equally: Johannes Geiselmann, Hidde de Jong. ✉ e-mail: hans.geiselmann@univ-grenoble-alpes.fr; hidde.de-jong@inria.fr

mass in *Escherichia coli*^{12,13}. The ribosomal growth law has been shown to hold over a large range of growth rates and for a wide variety of microorganisms, and has been generalized to cases of reduced translation rates by antibiotic treatment⁹ and different temperatures¹⁴. Simple mathematical models explain the growth law from basic hypotheses on cellular resource allocation, generally under the assumption that cells have evolved to maximize their growth rate^{9,11,14–21}.

The ribosomal growth law applies to populations of microorganisms in a state of balanced growth. In natural environments, however, growth is rarely balanced and microorganisms have to cope with regular changes in nutrient availability and other perturbations²². Theoretical models have predicted how microorganisms dynamically adapt the synthesis of ribosomes during shifts between balanced growth on a poor or a rich carbon source^{18,23,24}. A recent proteomics study reported changes in the (relative) abundance of ribosomes and other proteins during such upshifts and downshifts²³. This has motivated generalizations of the growth law to unbalanced scenarios, relating ribosomal protein fractions to observed jumps in growth rate after a nutrient upshift²⁵ (see also²⁶).

The quantification of ribosomal resource allocation on the single-cell level has not been attempted thus far. It is well-known, however, that individual cells within a microbial population do not behave identically, but display variable phenotypes^{27–33}. How do the resources allocated to the synthesis of ribosomal proteins, both during balanced and unbalanced growth, vary over the individual cells of an isogenic population? In order to answer this question, we constructed chromosomal reporter systems for monitoring ribosome expression in the model organism *Escherichia coli*. We measured the ribosome concentration in individual cells growing on a rich or a poor carbon source, as well as changes in ribosome concentration during upshifts and downshifts between these carbon sources, over extended periods of time (>80 generations). Moreover, we developed a method for the statistical inference of time-varying ribosome synthesis rates from the single-cell, time-course data thus acquired.

We found that, during balanced growth in a given medium, the bacteria display a wide variety of ribosome concentrations that are only weakly correlated with the single-cell growth rate. This would not be expected if bacteria had optimized costly ribosome expression to precisely match the protein synthesis rate required for a certain growth rate. During the upshift from a poor to a rich carbon source, we observed that cells with a higher pre-shift ribosome concentration more rapidly adapt their ribosome synthesis rate, but also the ribosome synthesis activity and the growth rate, to the new environment. We remark that these observations are consistent with the existence of a variable ribosome reserve which the bacterial cells may exploit to speed up adaptation to sudden changes in the environment^{25,26,34}.

In this study, we thus quantified, using a combination of reporter genes and statistical inference algorithms, dynamic investment in ribosomes on the single-cell level. The results reveal a surprising variability in the allocation of resources to ribosomes, the most costly molecular machine in bacterial cells, during both balanced and unbalanced growth. This raises fundamental questions on the role of the variability of ribosome concentrations in shaping the growth of a bacterial population and its adaptation to changing environments. Given the importance of growth and adaptation in biomedical and biotechnological applications, we expect our findings to have practical implications as well.

Results

Single-cell experiments to monitor changes in ribosome concentrations

In order to quantify the ribosome abundance in single *E. coli* cells, we tagged one of the ribosomal subunits with a green fluorescent protein (GFP). In particular, following previous work³⁵, we constructed on the

chromosome of the *E. coli* strain BW25113³⁶ a translational fusion of the *rpsB* gene, coding for the S2 subunit, and the gene encoding the fast-folding GFPmut2 (Methods). The resulting strain, expressing the fusion protein RpsB-GFPmut2, was called Rib.

We verified for the reporter strain, in batch experiments using a variety of different media, that the growth rates of the population are not significantly different from the corresponding growth rates of the wild-type strain (Fig. S1). Furthermore, we quantified in these experiments the fluorescence emitted by the cultures during balanced growth and normalized the fluorescence by the optical density, yielding a quantity proportional to the ribosome concentration on the population level. When plotting this quantity as a function of the growth rate, for the different conditions, we found a linear relationship in agreement with the growth law for ribosomes (Fig. S2). These control experiments demonstrate that the constructed reporter strain provides a reliable read-out of ribosome concentrations over a broad range of growth conditions.

In order to quantify ribosome concentrations in single cells, we used an experimental setup in which cells of the Rib reporter strain are grown in a mother machine and monitored using time-lapse fluorescence microscopy (Methods). Mother machines are microfluidics devices that allow cells trapped at the bottom of dead-end microchannels, so-called mother cells, to be followed over hundreds of generations in well-controlled conditions of growth³⁷. We submitted cells in the mother machine to upshifts from a poor growth medium (minimal medium with acetate) to a rich growth medium (minimal medium with glucose). After each upshift, the bacteria were left to grow for a sufficient number of generations (>10) to reach a state of balanced growth in the new medium. Each experiment consisted of at least two upshifts, separated by corresponding downshifts from glucose to acetate (Fig. S3). During these experiments, we acquired phase contrast and green fluorescence images at regular time-points (Methods and Supplementary Movies 1 and 2). Using existing image analysis software³⁸, we segmented the mother cells and recorded for each cell at each measurement time the cell length and the fluorescence intensity averaged over the segmented cell area (Fig. S4).

This experimental setup allowed us to monitor the concentration of ribosomes in single cells over long periods of time (several days) with high sampling density (measurement every 11–13 min). As illustrated in Fig. 1, the experiments reproduce a number of well-known features of *E. coli* growth. After the upshift from acetate to glucose, the cells are seen to divide faster, corresponding to the higher growth rate on glucose, the preferred carbon source of *E. coli*, and have a larger newborn cell length on average³². The fluorescence intensities increase after the upshift and stabilize at a higher level, reflecting that the higher growth rate on glucose comes with a higher ribosome concentration^{6,8,9}. Following the downshift, a lag phase is observed before the cells resume growth on acetate³⁹. These observations are reproducible in independent replicate experiments (Fig. S5).

Inference of time-varying ribosome synthesis rates

We exploited the data obtained from the mother machine experiments to quantify at the single-cell level how resources allocated to the synthesis of ribosomes vary over time, both during balanced growth and after a nutrient upshift or downshift. To this end, we first formulated a simple model describing the dynamics of the ribosome concentration in a mother cell (refs. 16,18 and Supplementary Note 1). The model assumes that the ribosome concentration evolves continuously in-between cell divisions. This is a reasonable approximation given (i) the high number of ribosomes in *E. coli* cells growing on glucose or acetate (between 8000 and 15,000^{8,12}), and (ii) the absence of evidence for discrete jumps in the ribosome concentration across cell divisions due to possibly uneven distribution of ribosomes over the two daughter cells (Fig. S6). The dynamics of the cellular ribosome

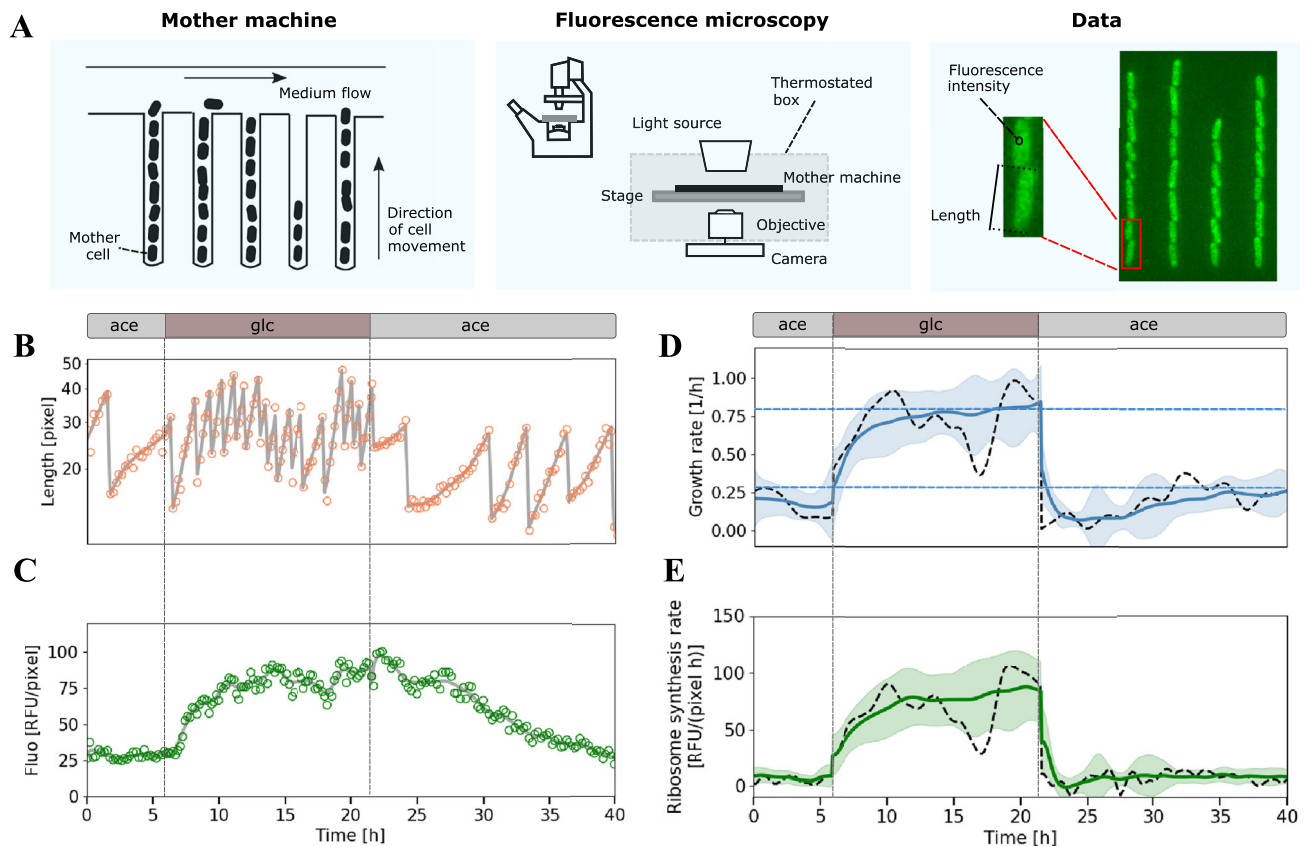


Fig. 1 | Measured and estimated quantities in mother machine experiments with a ribosomal reporter strain. **A** Schematic outline of the mother machine and the use of fluorescence microscopy to quantify cell length and fluorescence intensity over time. The fluorescence intensities of a cell reported in the text are the means of the intensities of pixels in the segmented cell area. **B**, **C** Cell length in log scale (orange dots) and green fluorescence intensity (green dots) of individual bacteria of the Rib strain, carrying a fusion of the ribosomal subunit S2 and the green fluorescent protein GFPmut2. The experiment consisted in several consecutive upshifts and downshifts (vertical dashed lines) between minimal medium with glucose (glc) or acetate (ace). **D**, **E** Cell length and fluorescence intensity measurements were used to estimate time-varying growth rates and ribosome

synthesis rates, respectively, using appropriate statistical inference methods (Methods). The gray solid curves in panels **B** and **C** represent the fits of the single-cell data obtained from the inference methods. The black dashed curves in **D** and **E** represent the corresponding estimates of the growth rate $\mu(t)$ and the ribosome synthesis rate $\nu_r(t)$ for this same mother cell. Blue and green solid curves represent the mean of the estimates over all cells considered in the experiment and confidence intervals are given as the standard deviation. The blue dashed lines in **(D)** represent the mean growth rates over all mother cells over the entire duration of the experiment (0.27 h^{-1} for acetate and 0.79 h^{-1} for glucose). Source data are provided as a Source Data file.

concentration r as a function of time t are defined in terms of the time-varying growth rate $\mu(t)$, the protein degradation rate γ , and the ribosome synthesis rate $\nu_r(t)$:

$$\frac{d}{dt}r(t) = \nu_r(t) - (\mu(t) + \gamma)r(t). \quad (1)$$

The model expresses that the instantaneous change in ribosome concentration arises from the difference between the rate of decay of ribosomes due to growth dilution and degradation ($(\mu(t) + \gamma)r(t)$) and the rate of synthesis of new ribosomes $\nu_r(t)$. The degradation constant γ is much smaller than the growth rates $\mu(t)$ considered here⁴⁰, so for simplicity, we assume that it is constant (Supplementary Note 1).

How do the data provided by the mother machine experiments, that is, the time-lapse measurements of the length and (average) fluorescence intensities of a cell, relate to the above model? In brief, the cell length measurements allow us to infer an estimate of the time-varying growth rate $\mu(t)$, in units $1/h$, while the fluorescence intensities report on the time-varying ribosome concentration, expressed in relative fluorescence units per pixel (RFU/pixel). Together with the measured degradation constant γ of the fusion protein⁴⁰, this information allows us to infer an estimate of $\nu_r(t)$, in units RFU/(pixel h).

In order to estimate single-cell growth rates from cell length data, we developed a dedicated method based on work from statistical signal processing (Methods and Supplementary Note 2). Like in other recent work on the estimation of single-cell bacterial growth rates (e.g.,^{41–44}), we do not assume that the latter are constant between two cell divisions. This is critical for monitoring medium shifts, when bacteria change their growth rate dramatically within one generation (Fig. S7). The method uses regularization to cope with measurement noise and discrete-time sampling of the data, thus penalizing overly rapid changes in growth rate. The regularization parameter was determined from the data by means of cross-validation. Figure 1B and D illustrate the estimation of the growth rate of a typical mother cell across an upshift and a downshift, and the corresponding fit to the length data. The mean growth rate over all mother cells considered in the experiment increases from $0.27 \pm 0.02 \text{ h}^{-1}$ on acetate to $0.79 \pm 0.03 \text{ h}^{-1}$ on glucose, in good agreement with values measured in batch for the BW25113 wild-type strain (0.28 h^{-1} and 0.78 h^{-1} , respectively⁴⁵, see also ref. 46).

For the estimation of single-cell ribosome synthesis rates, we formulated the inference of $\nu_r(t)$ from the growth-rate estimates and the fluorescence measurements as a Bayesian estimation problem and solved this problem by means of Kalman smoothing^{40,47}. The overall information flow of the procedure is summarized in Fig. 2, while more

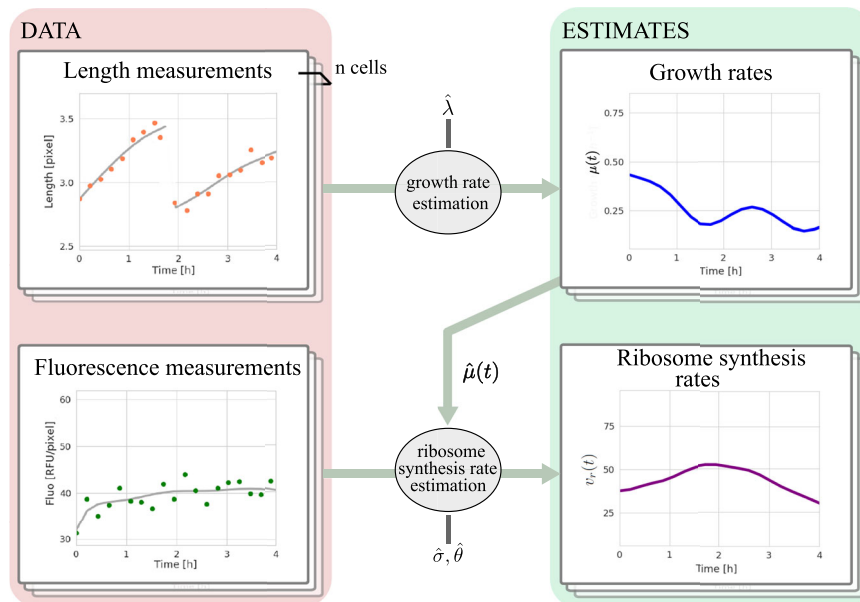


Fig. 2 | Inference procedures for estimating growth rates and ribosome synthesis rates from single-cell data. Time-lapse measurements of the length of mother cells are used as input by the growth-rate estimation method, returning time-varying estimates of the growth rate $\mu(t)$. The growth rate estimates $\hat{\mu}(t)$, along with time-lapse average fluorescence intensity measurements corresponding to overall intracellular ribosomal concentrations, are then used for the estimation of

single-cell ribosome synthesis rates $v_r(t)$. The two estimation methods rely on regularization to cope with measurement noise and return smoothed estimates. This requires values for the regularization parameters ($\hat{\lambda}$ and $\hat{\sigma}, \hat{\theta}$) which are estimated for each experiment to account for possibly different experimental conditions, machine settings, etc. (Methods and Supplementary Note 2).

details can be found in the Methods and Supplementary Note 2. The method uses a variant of the model of Eq. (1) that accounts for maturation of the fluorescent reporter. Ignoring maturation may distort the inference of synthesis rates, especially after a nutrient upshift or downshift⁴⁰. The maturation constant for the reporter used in this study, along with the estimation of the degradation constant, was determined in previous work⁴⁰. We checked that no correction for photobleaching was necessary (Methods). Similar to the estimation of growth rates, the inference of ribosome synthesis rates requires regularization parameters that were determined from the noise properties of the fluorescence intensity measurements for each experiment via a maximum likelihood approach. As a side product, the inference method also returns an estimate of the total ribosome concentration, that is, the sum of the concentrations of ribosomes tagged with a mature (observed) and immature (non-observed) fluorescent reporter (Methods).

Figure 1E shows the ribosome synthesis rate estimated for a single cell and Fig. 1C the corresponding predicted and observed fluorescence data for this cell. The figure also displays the mean ribosome synthesis rate estimated over all cells in the experiment. We observe that $v_r(t)$ immediately increases after the upshift from acetate to glucose and reaches a new, higher steady-state level quite fast. The higher value of $v_r(t)$ after the upshift means that the rate of synthesis of new ribosomes is higher during fast growth on glucose, consistent with the growth law stating that a higher growth rate requires a higher ribosome concentration^{8,9,48}. For the downshift, the dynamics of adaptation to acetate are also fast and involve a transient undershoot of the growth rate $\mu(t)$, which was also observed in previous work³⁹.

Variability of ribosome concentrations during balanced growth

The inference methods of Fig. 2 allowed us to estimate, for each of the individual mother cells, the time-varying growth rates $\mu(t)$, the (total) ribosome concentrations $r(t)$ and the ribosome synthesis rates $v_r(t)$ from the microfluidics data. The estimations are performed over the whole time course of the experiment, both during balanced and

non-balanced growth. During balanced growth, the ribosome concentration is expected to reach steady state, which implies $v_r/r = \mu + \gamma$, up to stochastic noise (Eq. (1)). In order to verify if the estimates agree with this equality, we computed during balanced growth on glucose and acetate (more than 5 generations after an upshift or downshift), for every individual mother cell and over each generation, the average growth rate and the average ratio of ribosome synthesis rate and ribosome concentration. The results, consisting of more than 800 data points for individual generations of individual cells are shown in the scatter plot of Fig. 3A. The quantities are strongly correlated ($R^2 = 0.94$), confirming that the method is capable of recovering the expected relationship between r , v_r , and μ during balanced growth.

The balanced growth data enable the direct test of an important empirical relationship in microbial physiology, the growth law for ribosomes. The linear increase of the ribosome concentration with the growth rate, predicted by the growth law, has been extensively studied for populations of bacteria grown in different media^{4–11}. Nothing is known, however, about the correlation of the ribosome concentration with the growth rate in individual cells grown in the same medium. While one might expect the ribosomal growth law to hold for this case as well, the test on the single-cell level of another population-average growth law, relating newborn cell volume to growth rate, shows that some caution is warranted. Taheri-Araghi et al.³² found strong quantitative deviations from the expected exponential dependence of newborn cell volume on growth rate for individual cells grown in the same medium (see⁴⁹ for a related discussion confronting the population-average model of cell-cycle progression with single-cell data).

We first ascertained that the growth rates and ribosome concentrations averaged over individual generations of individual cells in balanced growth on acetate or glucose are consistent with the growth law established from population-level measurements (Fig. 3B). We then plotted the growth rates and ribosome concentrations of each individual cell in the two media (Fig. 3C). While the overall trend in the

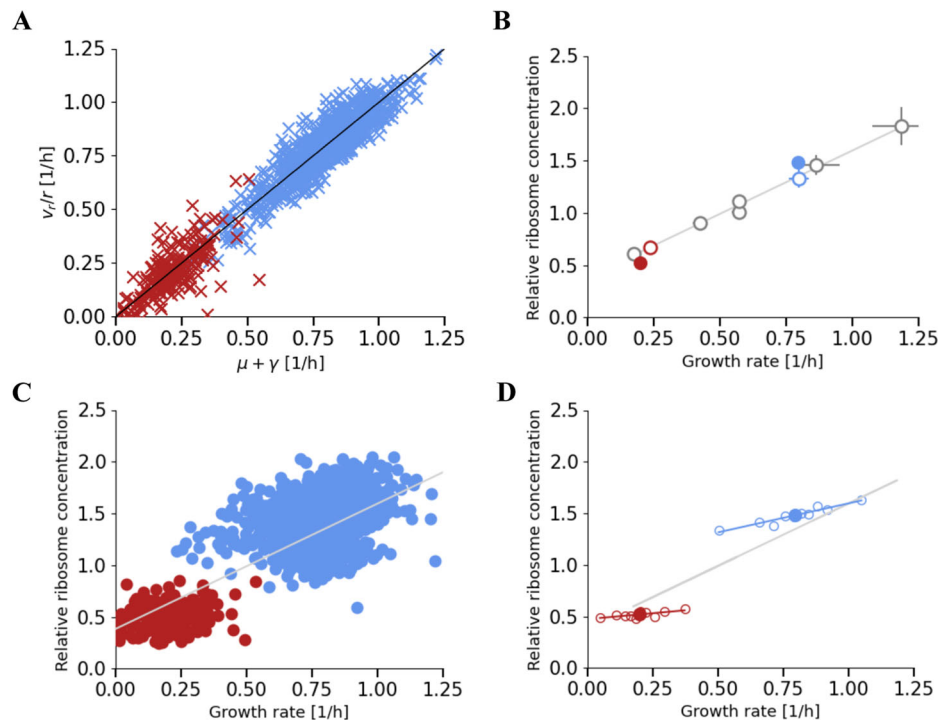


Fig. 3 | Investment in ribosomes on the single-cell level during balanced growth. **A** Verification of balanced growth conditions for selected data from the microfluidics experiment in Fig. 1. Each cross corresponds to the computed values of $\mu + \gamma$ and v_p/r for an individual generation of an individual mother cell of the Rib strain growing on acetate (red) or on glucose (blue) for at least five generations. The data points are concentrated around the diagonal ($R^2 = 0.94$), indicating that the method is capable of reproducing the expected relationship between the quantities during balanced growth. **B** Relation between the mean of the growth rates μ and the mean of the total ribosome concentrations r for the balanced growth dataset from panel A (filled circles). The microfluidics data are compared with population-level measurements for the same strain growing in batch on glucose, acetate, or other carbon sources (open circles) (Fig. S2). Data points for acetate are colored in red, for glucose in blue, and for other carbon sources in gray. In order to make the two data sets comparable, all ribosome concentrations were normalized by the mean of the ribosome concentrations for glucose and acetate. A line was fitted to the batch

data and plotted as a visual aid. Each point is the mean of 5 replicates and confidence intervals are given by two times the standard error of the mean. The growth rates and the relative ribosome concentrations during growth on glucose and acetate agree between the batch growth and microfluidics datasets. **C** Relation between ribosome concentrations and growth rates of individual generations of individual cells from the balanced growth dataset from panel A (data points for acetate in red, data points for glucose in blue). While the line fitted to the data in panel B, shown for reference, captures the global trend in the data ($R^2 = 0.64$), the variability of single-cell ribosome concentrations is important. **D** As in panel C, but after discretizing the data points for glucose and acetate into ten equal-sized bins. Within each growth condition, the ribosome concentration across individual cells weakly depends on growth rate, as quantified by the slope of the straight line fitted to the binning points (0.56 ± 0.06 for glucose and 0.22 ± 0.08 for acetate), which is much smaller than the slope of the growth law in panel B (1.2 ± 0.04). Source data are provided as a Source Data file.

data is captured by the population-level growth law ($R^2 = 0.64$), we also observe a huge variability of growth rates and ribosome concentrations, especially when focusing on cells grown in either glucose or acetate. In particular, individual cells grown in the same medium can grow fast with low ribosome concentrations or slow with high ribosome concentrations. When analyzing the relation between the single-cell ribosome concentrations and growth rates for each condition separately (Fig. 3D), we still find a linear dependency but much weaker than for the overall population-level growth law. Similar results were obtained in an independent replicate experiment (Fig. S8). We also found a large variability of the single-cell ribosome synthesis rates when plotted against the growth rate (Fig. S9).

How can the large variability of ribosome concentrations across individual cells in a population be explained? Further development of the model of Eq. (1) yields the following expression, relating the growth rate and the ribosome concentration during balanced growth (refs. 16,23,50 and Supplementary Note 1):

$$\epsilon \delta r = (\mu + \gamma) \frac{\eta}{\beta}. \quad (2)$$

Both sides of this equation are expressions of the total protein synthesis rate v_p . The left-hand side decomposes the protein synthesis

rate as the product of the concentration of actively translating ribosomes (δr) and the translation elongation rate (ϵ). The right-hand side defines the protein synthesis rate as compensating, during balanced growth, for the loss of protein due to growth dilution and degradation. This loss term is proportional to the product of the biomass density ($1/\beta$) and the protein fraction of biomass (η), which equals the total protein concentration $p = \eta/\beta$ (Supplementary Note 1). All of the above quantities relating μ to r may vary across individual cells in the population.

Eq. (2) helps explaining that, for a given growth rate, we may find a range of ribosome concentrations across individual cells of a population in balanced growth. For example, one cell may have a higher ribosome concentration than another (higher r), but if translation advances at a lower elongation rate (lower ϵ), it may not grow faster (no higher μ). Alternatively, a given growth rate may be attained for a range of ribosome concentrations r if individual cells differ in the total protein concentration ($p = \eta/\beta$). Much experimental work has gone into the quantification of the factors in Eq. (2) on the population level^{2,25,48,51–58}. However, very little is known about their variability across individual cells in a population (Discussion).

The weak correlation between growth rates and ribosome concentrations of single cells growing in the same medium, observed in Fig. 3D, is surprising in the light of the hypothesis, exploited in

mathematical models^{11,14,15,18–20,59,60}, that bacteria have evolved to optimize their growth rate. One would expect growth-rate maximizing cells to tightly control their investment in costly ribosomal machinery and avoid wasting resources on unused or underused protein synthesis capacity⁶¹. However, while suboptimal from the perspective of growth-rate maximization during balanced growth, the maintenance of excess protein synthesis capacity may be beneficial in other ways. It has been suggested, for example, that a reserve of inactive ribosomes can be exploited for rapid adaptation to environmental changes and thus confer a fitness advantage^{25,26,34,58,62–64}.

Variability of adaptation of ribosome synthesis after a nutrient upshift

In order to test a possible role of the observed variability of ribosome concentrations in the response to a change in environment, we analyzed the response of single cells to a nutrient upshift or downshift. As explained above, during balanced growth the ribosome concentrations and ribosome synthesis rates are coupled through the relation $v_r = (\mu + \gamma)r$ (Eq. (1)), that is, on average the rate of synthesis of new ribosomes compensates for degradation and growth dilution of ribosomes so as to keep the ribosome concentration constant. This is no longer true during a nutrient upshift or downshift, when the terms in the above equation may temporarily diverge until a new state of balanced growth is attained (Fig. S10).

We first computed the average over all mother cells of the estimated ribosome synthesis rate $v_r(t)$ after an acetate-glucose upshift (Fig. 4A). Immediately after the upshift, the mean ribosome synthesis rate $v_r(t)$ jumps to a higher value and then gradually increases to a new steady state, corresponding to balanced growth on glucose. The growth rate $\mu(t)$ displays a similar response, a jump followed by a gradual increase to the new steady state (Fig. 4B). The ribosome concentration $r(t)$ increases more slowly to the steady state (Fig. 4C), buffering the rapid changes in ribosome synthesis rate and growth rate (Eq. (1)). The above average adaptation profiles are consistent with previous population-level measurements^{2,23–26,34,65–67}. The data also allow the computation of the ribosome synthesis activity, defined as the ratio $v_r(t)/r(t)$ (Supplementary Note 1), averaged over all mother cells. Ribosome synthesis activity jumps to a new constant value directly after the upshift (Fig. 4D). This jump in synthesis activity has also previously been reported on the population level, though not quantified in such detail as here^{24,34,68}.

How does the observed response to a nutrient upshift vary across the individual cells? Interestingly, when considering for every mother cell the average ribosome synthesis rate as well as the average growth rate over the first two hours after the upshift, we see that the two are correlated (Pearson correlation coefficient $\rho = 0.75$, Fig. 4E). That is, cells that more rapidly increase their ribosome synthesis rate also increase their growth rate more rapidly. A generalization of Eq. (2) to the case of unbalanced growth predicts a linear relation between the temporally-varying growth rate $\mu(t)$ and ribosome synthesis rate $v_r(t)$ (Supplementary Note 1):

$$\frac{d}{dt} \left(\frac{\eta(t)}{\beta(t)} \right) + (\mu(t) + \gamma) \frac{\eta(t)}{\beta(t)} = \frac{v_r(t)}{\alpha(t)} \quad (3)$$

The relation between $\mu(t)$ and $v_r(t)$ thus depends on changes in other physiological characteristics occurring directly after an upshift. In particular, the product of the total biomass concentration $1/\beta(t)$ and the protein fraction of biomass $\eta(t)$, equal to the total protein concentration $p(t)$, is expected to slightly decrease on average when shifting from balanced growth on a poor to a rich carbon source^{48,55,56}, whereas the fraction of the protein synthesis rate allocated to ribosomes $\alpha(t)$, equal to the ribosomal protein fraction during balanced growth, is expected to increase^{9,12,13}. These factors may vary across

individual cells and thus confound the correlation between growth rate and ribosome synthesis rate reported in Fig. 4E.

The immediate response of the ribosome synthesis rate is a good indicator of the adaptation of the allocation of cellular resources to ribosomes following a change in environment, but the individual time-courses of $v_r(t)$ after the upshift are noisy (Fig. S11). In order to discern a pattern in the data, we therefore clustered the cells into two groups of faster and slower adapters of the ribosome synthesis rate (Fig. S12, see Methods for details). It is important to emphasize that the clustering was done for visualization purposes and that we do not claim that the observed continuum of cellular responses in Fig. 4E can be captured by distinct groups of fast and slow adapters. Figure 4F, G shows the average response to a nutrient upshift for the two groups. Interestingly, while the speed of the response differs, the magnitudes of the ribosome synthesis rates and growth rates before and after the upshift, once a new state of balanced growth is attained, are very similar. That is, on average, faster and slower adapters are producing ribosomal proteins at a higher rate and growing faster during, but not before or after the adaptation process. This conclusion equally applies to a second upshift in the same experiment and to an upshift in an independent replicate experiment (Fig. S13–S14).

The grouping of the cells into faster and slower adapters also helps to bring out another interesting pattern, confirmed in the replicate experiments. Right before the upshift, cells that adapt faster appear to have a higher ribosome concentration and maintain this higher concentration after the upshift (Fig. 4H and Fig. S13–S14). We confirmed that this difference is statistically significant (Fig. S15). The higher ribosome concentration before the upshift is consistent with a higher ribosome synthesis rate after the upshift, given the definition of the latter as $v_r(t) = \alpha(t)v_p(t)$ (Supplementary Note 1), which with Eq. (2) yields

$$v_r(t) = \alpha(t)\epsilon(t)\delta(t)r(t) \quad (4)$$

However, the gradual adaptation of the ribosome concentration cannot account for the jump in ribosome synthesis rate directly after the upshift^{24,34}. When considering the ribosome synthesis activity $v_r(t)/r(t) = \alpha(t)\epsilon(t)\delta(t)$, which factors out the direct effect of the higher ribosome concentration, we see that the synthesis activity jumps to a higher level in faster cells (Fig. 4I), consistent with the higher jump in ribosome synthesis rate. In other words, faster adaptation of the ribosome synthesis rate involves higher synthesis activity of the ribosomes directly after the upshift, as confirmed by the strong correlation of these quantities ($\rho = 0.86$, Fig. S16).

According to Eq. (4), the observed higher jump in ribosome synthesis activity in faster adapters may be due to differences in the reallocation of ribosomes to the synthesis of ribosomal proteins (α), adaptation of the translation elongation rate (ϵ), or adjustment of the fraction of active ribosomes (δ). Our data do not allow to relate the variability of the response of ribosome synthesis activity to any of these factors specifically. However, the model suggests possible explanations and further experiments (Supplementary Note 3 and Discussion), notably exploiting the observation that faster adaptation of the ribosome synthesis rate comes with a higher ribosome concentration before the upshift. Previous work proposed a dynamic growth law relating the magnitude of the jump in growth rate directly after an upshift to the difference in ribosome concentrations during balanced growth on a rich and a poor carbon source²⁵. While the population-averaged data from the microfluidics experiments are consistent with the predictions of the dynamic growth law, the latter cannot explain the observed variability on the single-cell level (Fig. S18).

We performed the same analysis of the adaptation of the cellular investment in ribosomes for a glucose-acetate downshift. The average ribosome synthesis rate $v_r(t)$ and growth rate $\mu(t)$ sharply drop directly

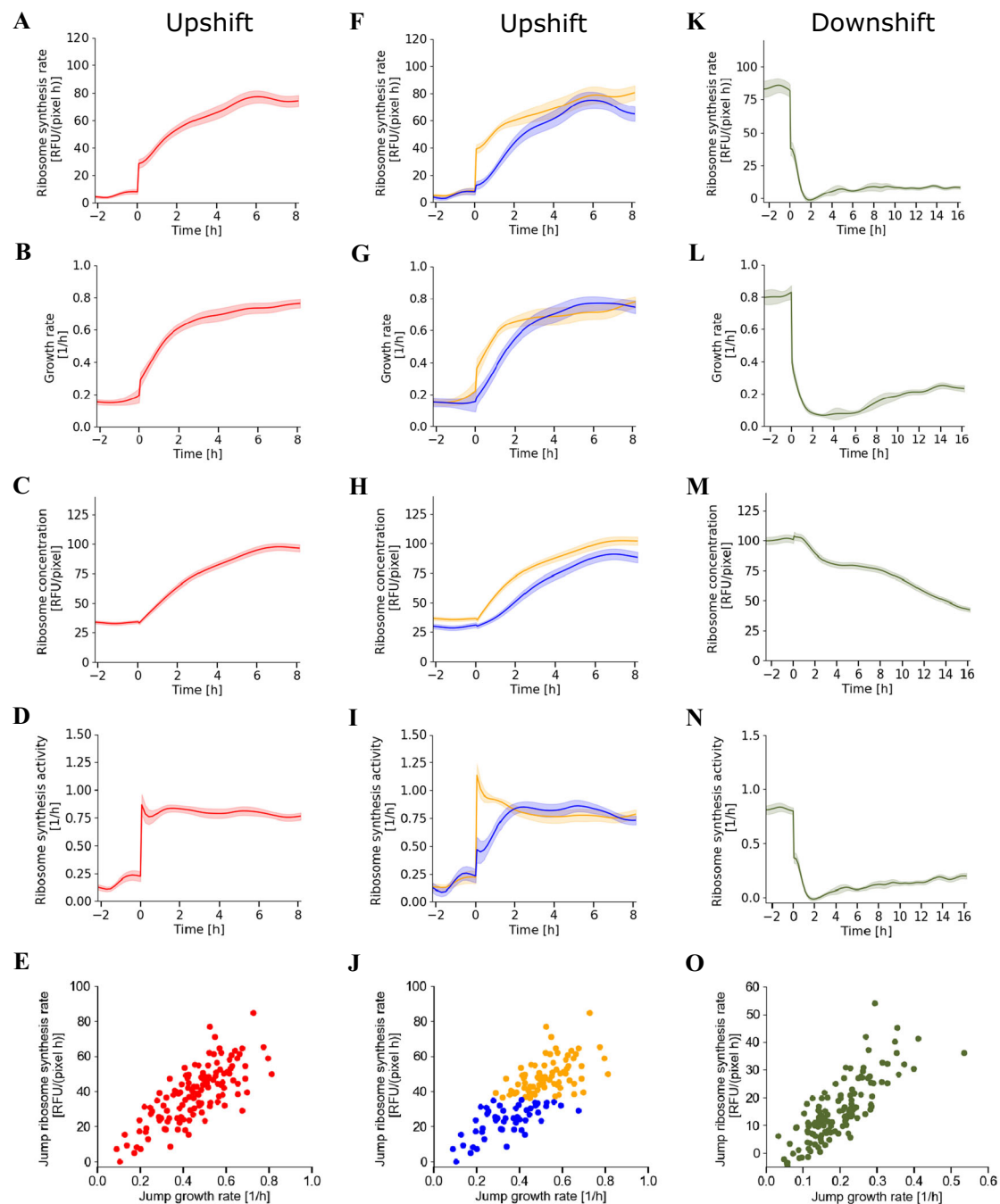


Fig. 4 | Adaptation dynamics of investment in ribosomes after a nutrient upshift and downshift. **A–D** Mean adaptation of the ribosome synthesis rate $v_r(t)$, growth rate $\mu(t)$, ribosome concentration $r(t)$, and ribosome synthesis activity $v_r(t)/r(t)$ after an acetate-glucose upshift applied to the Rib strain growing in a mother machine (Fig. 1). The above quantities were estimated from the data for different mother cells using the inference methods of Fig. 2 and averaged over 129 cells. The time-courses show a distinct jump in ribosome synthesis rate, growth rate, and ribosome synthesis activity directly after the upshift. **E** Correlation of the single-cell ribosome synthesis rates and growth rates (red dots), averaged over the first two hours after the upshift. The Pearson correlation coefficient ρ equals 0.75. **F–I** Clustering of the single-cell ribosome synthesis rates after the upshift using k-means (Methods) illustrates the different behavior of

faster adapters (orange, 77 cells) and slower adapters (blue, 52 cells). Faster adapters have a significantly higher ribosome concentration before (and after) the upshift (Fig. S15). **J** Like in panel E, but indicating the cells included in the cluster of faster (orange) and slower (blue) adapters. **K–N** As in panel A–D, but for a glucose-acetate downshift carried out in the same experiment (130 cells). The average adaptation time-course displays an undershoot of the ribosome synthesis rate, growth rate, and ribosome synthesis activity before settling at the steady-state value for growth on acetate, while the ribosome concentration decreases more gradually. **O** Correlation of the single-cell ribosome synthesis rates and growth rates (green dots), averaged over the first two hours after the downshift ($\rho = 0.81$). Confidence intervals in the above plots are given by two times the standard error of the mean. Source data are provided as a Source Data file.

after the downshift, before partially recovering and eventually settling at the lower growth rate and ribosome synthesis rate characteristic for growth on acetate (Fig. 4K–L, compare with Fig. 3). Ribosome synthesis activity $v_r(t)/r(t)$ responds similarly, while the ribosome

concentration more slowly attains a lower level (Fig. 4M, N). The drop in ribosome synthesis rate and growth rate are correlated ($\rho = 0.81$, Fig. 4O), but there is little variation in the adaptation dynamics of the ribosome synthesis rate across the individual cells, in this and in a

replicate experiment (Fig. S17). The plots suggest that the immediate drop in ribosome synthesis rate $v_r(t)$ after the downshift, and its partial recovery after a few hours, is driven by the dynamics of the ribosome synthesis activity $\alpha(t)$, $\epsilon(t)$, $\delta(t)$. A plausible hypothesis is that the rapid disappearance of glucose after the downshift depletes precursor pools (and thus decreases the translation elongation rate $\epsilon(t)$) and provokes regulatory responses affecting the proportion of ribosomes actively translating ribosomal proteins ($\alpha(t)$ and $\delta(t)$). The adaptation of the cells to acetate partially reverses these effects.

Discussion

The ribosomal growth law empirically describes the allocation of cellular resources to ribosomes, macromolecular machines occupying a central place in the growth economy of microbial cells. The growth law has been verified for many species and experimental conditions, yet its scope has been mostly limited to balanced growth. A few studies have focused on growth in unbalanced conditions, especially the adaptation of ribosomal resource allocation after a sudden change in nutrient availability^{18,23,24}, but experimental data remain scarce. Moreover, the available data quantify adaptation on the population level, thus ignoring possible heterogeneous behavior of the individual cells making up the population^{27–33}. The question that remains unanswered is therefore how the investment in ribosomes varies across the cells in an isogenic population, both during balanced and unbalanced growth in a given medium.

In this study, we addressed the above question by quantifying ribosomal resource allocation on the single-cell level. We created fusions of a ribosomal subunit with different fluorescent reporters in *E. coli* and conducted time-lapse microfluidics experiments in which we recorded the dynamic adaptation of the abundance of the tagged ribosomes after a sudden change in carbon source (Fig. 1). Moreover, we developed a robust statistical inference method to reconstruct the ribosome synthesis rate from the resulting fluorescence data, using a mathematical model taking into account protein synthesis, maturation, degradation, and growth dilution (Fig. 2). The method states the reconstruction of the ribosome synthesis rate as a Bayesian optimization problem and solves this problem within the classical framework of Kalman filtering and smoothing⁶⁹. Smoothing is achieved by automatic, data-determined tuning of regularization parameters that are defined on the level of the quantity to be estimated, the ribosome synthesis rate. This does not require a-priori smoothing of the data and propagation of the smoothed data through the model, thus avoiding difficult-to-control estimation errors⁷⁰. The method is generic and applicable to other microorganisms and experimental scenarios, not only for ribosomes but for any protein tagged with a fluorescent reporter.

We first explored the relationship of the growth rate and the ribosome concentration during balanced growth on glucose or acetate (Fig. 3). Whereas the averaged data agree with the well-established growth law for ribosomes, which posits a linear dependence of the ribosome concentration on growth rate across different media, we discovered that there exists a much weaker correlation between ribosome concentration and growth rate across individual cells growing in the same medium. A simple model of the dynamics of ribosome concentrations allows the formulation of hypotheses on the origin of the high variability of ribosome concentrations during balanced growth (Eq. (2)). Individual cells growing in the same medium may differ in the translation elongation rate ϵ , the fraction of actively translating ribosomes δ , the total biomass density $1/\beta$, and the protein fraction of biomass η .

The above factors have been extensively quantified on the population level. The translation elongation rate was long considered constant for bacteria growing in different media⁷¹, but recent experiments with *E. coli* have established that ϵ varies about two-fold over a range of fast- and slow-growth conditions⁵⁷, confirming previous

reports^{51,54}. Careful measurements on the population level have shown that, in the conditions considered here, on average about 10% of ribosomes in the *E. coli* cell are inactive⁵⁷, and thus form an unused ribosome reserve^{25,34,58}. The higher the ribosome reserve, the lower the value of δ . While the population-averaged total biomass density $1/\beta$ is approximately constant for bacterial cells in balanced growth over a range of conditions^{52,53,56}, the protein fraction η is known to vary considerably, from 65% for growth in a poor medium to 76% in a rich medium (ref. 56, see also refs. 48,55).

Apart from the bacterial biomass density^{72–74}, very little of the above information is available on the single-cell level. Techniques for quantifying gene expression in individual bacterial cells, however, have become widespread. This has notably allowed the discovery of a large variability in the abundance of specific (reporter) proteins across microbial cells growing in identical conditions^{75–79}. Exploiting a previously established relationship between growth rate and expression of specific genes on the population level, recent work predicted growth rates for individual yeast cells from single-cell RNA sequencing data and correlated these growth rates with the measured expression levels of ribosomal genes⁸⁰. The authors found that the population-level growth law accounted for only a small fraction of the observed variability in single-cell expression levels, like in Fig. 3 of this work. A recent theoretical study predicted that, during balanced growth, fluctuations in enzyme rather than ribosome concentrations could account for the variability of growth rates of individual cells⁸¹. This is consistent with previous experimental work, where a causal connection between expression fluctuations of catabolic enzymes and the growth rate of single *E. coli* cells was established⁴². The latter studies point to a possible extension of our analysis. In addition to considering correlations between growth rates and ribosome concentrations within a single generation (Fig. 3C), correlations between these variables along lineages of mother cells could be considered. This might reveal patterns in the joint variability of ribosome concentrations and growth rates over longer time-scales^{79,82–84}.

The observed variability of ribosome concentrations during balanced growth could be an unavoidable consequence of the stochasticity of gene expression^{85–87}, without a specific biological function. In particular, individual cells may not have the capacity to precisely control the factors influencing the ribosome synthesis rate v_r . For example, the allocation of protein synthesis capacity to the production of new ribosomes in *E. coli*, quantified by the factor α , is regulated by the signaling molecule guanosine tetraphosphate (ppGpp)^{88–92}. If the activity of the enzymes responsible for ppGpp synthesis and hydrolysis is heterogeneous across a population of cells, then the number of molecules of ppGpp may diverge, giving rise to variability of α , and hence v_r (Eq. (4)). Despite the fact that *E. coli* may thus experience fundamental limits on the regulation of resource allocation on the single-cell as compared to the population level, the large differences in ribosome contents of the individual bacteria, up to three-fold, remain surprising. Ribosomes are costly, abundant protein complexes, highly conserved in evolution, and responsible for the synthesis of proteins, the major component of biomass. Moreover, a high ribosome concentration in a mother cell tends to be preserved over more than 10 generations (Fig. 4), which would not be expected if the observed variability was due to random gene expression noise alone.

Alternatively, the variability of ribosome concentrations could have a biological function, analogously to what was demonstrated in various examples of bacterial stress responses^{27,28,31,93}. The maintenance of excess ribosomes in a ribosome reserve could confer a fitness advantage to cells in an isogenic population, by trading off maximal growth during balanced growth against the capacity to quickly react to an environmental change^{25,26,34,58,62–64}. In order to investigate this possibility, we also considered the allocation of resources to ribosomes in dynamic conditions, in particular after an

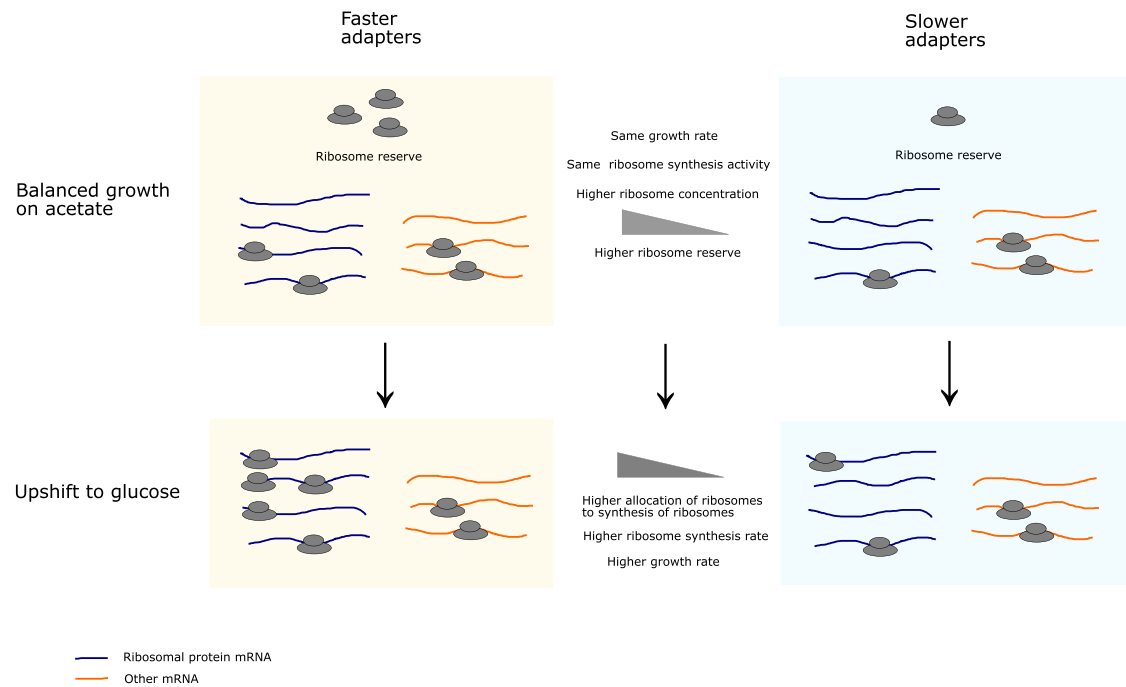


Fig. 5 | Explanation for the occurrence of faster and slower adaptation of ribosome synthesis after a nutrient upshift. Faster adapters have a higher ribosome concentration than slower adapters before the upshift from acetate to glucose (Fig. 4H). This presumably allows them to have a higher ribosome reserve, that is, a higher excess capacity that can be allocated to the synthesis of new ribosomes

immediately after the upshift. This allows faster adapters to make a higher jump in ribosome synthesis rate after the upshift (Fig. 4F), and therefore growth rate (Fig. 4G). Supplementary Note 3 mathematically develops the above reasoning in the context of the model used for the inference and analysis of the ribosome synthesis rates.

upshift from a carbon source sustaining a low growth rate (acetate) to a carbon source enabling a high growth rate (glucose). Our results show a large variability in the responses of individual cells (Fig. 4 and Fig. S13–S14). Whereas some cells quickly adapt their ribosome synthesis rate to the level expected for growth on glucose, others do so more slowly. The jump-like adaptation of ribosome synthesis after the upshift is consistent with previous models^{23,24}, but does not agree with the oscillatory patterns predicted for optimal biomass accumulation¹⁸. Some reports do suggest oscillations in the synthesis rate of ribosomal proteins immediately after an upshift^{66,94}, but on a time-scale that is too short to be observed in our experiments. Most strikingly, the speed of adaptation of the ribosome synthesis rate, which seems to be the consequence of a sudden increase of ribosome synthesis activity, is correlated with that of growth rate.

Our data show that, on average, cells that adapt faster also have a higher ribosome concentration before the upshift (Figs. 4 and S15). This suggests that a higher ribosome concentration may speed up the response to a nutrient upshift. The simple model used in this study allows the formulation of causal hypotheses that make this suggestion more precise (Supplementary Note 3). The basic arguments are summarized in Fig. 5. Given that before the upshift, the faster and slower adapters have on average the same ribosome synthesis activity and growth rate (Fig. 4), a higher pre-shift ribosome concentration allows a larger fraction of the ribosomes to remain inactive. Assuming that the entire ribosome reserve is allocated to protein synthesis directly after the upshift, the faster adapters with the higher ribosome reserve have the opportunity to allocate a larger fraction of the available ribosomes to the synthesis of ribosomal proteins, thus enabling on average a higher jump of the ribosome synthesis rate. The above reasoning can be further refined by taking into account that the total protein concentration and the translation elongation rate may also vary between individual cells (Supplementary Note 3). Testing the above explanatory hypotheses requires direct or indirect

quantification of the activity of ribosomes in vivo and on the single-cell level (Supplementary Note 3), which despite steady technological advances remains an arduous task today.

In conclusion, the present work identifies an important source of cellular heterogeneity on the level of ribosomes, the molecular machines at the heart of cellular self-replication. We have provided some arguments for attributing a physiological significance to the large variability of ribosome concentrations, based on the observation that on average, a higher ribosome concentration speeds up the response of the ribosome synthesis rate and therefore the growth rate after a nutrient upshift. It should be added though, that there is no evidence for a bet-hedging strategy trading off faster adaptation after a nutrient upshift against lower pre-shift growth rate. On average, faster and slower adapters have the same growth rate before the upshift (Fig. 4). Further experiments that take into account a larger range of environmental scenarios are necessary to establish the ecological relevance of our findings. The results of this study nevertheless provide concrete leads to address the fundamental question whether *E. coli* cells have evolved to exploit or merely tolerate the variability in ribosomal resource allocation^{95,96}.

Methods

Strain construction

The strain used in this study were derived from the *E. coli* K12 strain BW25113³⁶ where the *fhuA* gene was deleted by homologous recombination to confer resistance to phage infections⁹⁷. To visualize the ribosomes, we used a construction similar to the one described by Bakshi et al.³⁵ where the gene coding for the green fluorescent protein GFPmut2⁶⁰ was fused to the C-terminus of *rpsB*, the gene coding for the S2 ribosomal subunit, via a flexible linker of three amino acids (LEI).

The cloning procedure consisted in first amplifying a PCR fragment carrying 50 bp of sequence identity with the target insertion site. The PCR fragment, called (positive-negative selection) “cassette”, contains two divergently transcribed genes: the gene coding for

resistance to kanamycin, transcribed from a constitutive promoter, and the gene coding for the toxin CcdB, transcribed from the arabinose-inducible promoter pBAD⁹⁸. This fragment was recombined into the target site using the pSIM plasmid that provides the lambda Red recombination functions⁹⁹. The successful insertion was selected on LB containing glucose and kanamycin. Glucose prevents expression of the CcdB toxin and kanamycin selects for the presence of the cassette on the chromosome. In a second recombination step, the cassette was removed by recombination of a PCR fragment containing the sequence to be integrated flanked by the same 50 bp homology regions to the target site. Successful recombination is selected on LB containing 1% arabinose. Arabinose activates the pBAD promoter, and therefore the expression of the toxin CcdB, if the cassette is still present on the chromosome. A successful recombination will have removed the cassette and thus allow the growth of the strain in the presence of arabinose. The resulting strain was called Rib, for ribosomal reporter.

The strain used in this study is defined in Table S1 and graphically presented in Fig. S19. The construction was verified by sequencing of the modified chromosomal region. The following primers (5'-3') were used: AAGAAGCAAACAACCTGG (forward), AAAAGTAAAAAGGGGGC (reverse).

Growth media

For all experiments, we used M9 minimal medium¹⁰⁰ supplemented with vitamin B1 (5 mg/L) and mineral trace elements. Pre-cultures for the microfluidics experiments were prepared in the above medium supplemented with 2 g/L of acetate and 0.1 g/L of bovine serum albumin (BSA). The medium used for the microfluidics experiments was supplemented with 2 g/L of acetate or glucose. The experimental conditions of the individual microfluidic experiments are detailed in Table S2.

For strain validation in batch experiments, minimal medium was supplemented with 2 g/L of one of the following carbon sources: D-glucose, acetate, D-xylose, pyruvate, glycerol, D-fructose, D-galactose and maltose. Furthermore, 2 g/L of casamino acids were added to D-glucose and glycerol in separate conditions. For pad experiments, the medium was supplemented with 2 g/L of acetate before adding agarose.

Batch growth experiments

All strains were streaked from the freezer stock on LB agar plates several days prior to the experiments. Overnight cultures were grown by inoculating a single colony in liquid minimal medium supplemented with specified carbon sources. Bacterial growth for all experiments occurred at 37 °C and liquid cultures were shaken at 200 rpm.

Overnight cultures of the wild-type and reporter strain were diluted into a 96-well microplate at an OD₆₀₀ of 0.02 where each well contained the same medium as used for the preculture. 2 mm glass beads were added in each well to improve oxygenation. The bacteria were left to grow for up to 24 hours at 37 °C in a Tecan Infinite 200M plate reader, while monitoring the absorbance and green fluorescence.

Outliers in the absorbance and fluorescence curves due to the light reflection by the beads were filtered using WellInverter¹⁰¹. The fluorescence background was corrected by subtracting the fluorescence emitted by the wild-type strain in the same conditions. The absorbance curves were corrected by subtracting the background of a well-containing medium but no bacteria. The growth rate during balanced growth of the population was estimated directly from the absorbance curves, using the method described by Zulkower et al.⁷⁰. In order to obtain a proportional estimate of the reporter protein concentration during balanced growth, the background-corrected fluorescence curves were divided by the background-corrected absorbance curves.

Microfluidics experiments

Fabrication of microfluidic devices. The master-molds were obtained from Epsilon Micro Devices (College of Engineering, Zahn Center, 5500 Campanile Drive, San Diego CA). In order to produce PDMS mother machines, with microchannels of dimensions 25 × 1.2 × 1.3 μm, we adapted the protocol from the mother machine handbook published by the Jun laboratory at UC San Diego (<https://jun.ucsd.edu/files/mothermachine/mothermachinehandbook.pdf>). In particular, we mixed a curing agent and polymer base at a 1:10 ratio (Sylgard Elastomer Kit 184). The mix was poured into the mold and trapped air bubbles were removed in a vacuum chamber. The resulting devices were cured for a minimum of 2 hours at 65 °C. Devices were then removed from the master-mold and a 0.75 mm punch was used to create the inlet and the outlet. Before use, the devices were treated with pentane and acetone and were left to dry overnight. A plasma cleaner (PDC-32G Harrick Plasma) operated at high intensity for 40 seconds was used for surface activation of the devices and previously cleaned microscope slides. Each device was placed on a microscope slide and then put at 65 °C for 10 minutes. 50 mg/mL of BSA was injected into the sealed devices for surface passivation and the devices were then incubated at 37 °C for 1 hour.

Device loading and medium shifts. Precultures were performed in the same way as for the batch growth experiments described above. The optical density of strains growing in minimal medium with acetate was monitored and the cells were harvested during balanced growth (after at least 6 generations). The cells were then washed with fresh medium containing 50 mg/mL of BSA, concentrated around 100-fold and loaded into the device. The individual cells growing in the microchannels were left overnight in acetate to reach balanced growth before starting image acquisition.

An Elveflow pressure controller (OB1 MK3) equipped with a microfluidic flow sensor (0 to 50 μL/min) was used to assure a constant flow delivery of 20 μL/min to the device. The bottles of medium to be changed at the time of medium switches were prepared and put at 37 °C many hours before the switch. After the switch, 2 to 3 minutes were required for the new medium to reach the device. The corresponding dead-volume and dead-time were taken into account in all our analyses. Figure S3 illustrates the scenario for a typical microfluidics experiment.

Image acquisition. A Zeiss Axio Observer Z1 inverted microscope equipped with a halogen lamp controlled by a Vincent D1 shutter and a motorized xy-stage was used to perform the experiments. The focus was maintained by Zeiss Definite Focus. Images were recorded using a Zeiss Plan-APOCHROMAT 63x/1.40 oil objective and a Digital CMOS camera (Hamamatsu Orca-Flash 4.0). A constant temperature of 37 °C was ensured by a Peltier-equipped box with temperature sensors. The setup was controlled by the Micromanager software¹⁰² and images were recorded using the Multi-Dimensional Acquisition (MDA) feature. A phase contrast image (70 ms exposure) was recorded along with a (green) fluorescence image every 11-13 minutes for multiple positions in the device. To obtain fluorescence images, a Zeiss Colibri 7 was used equipped with LEDS fixed at 6% intensity. The following filter, purchased from Chroma, was used: GFP (49002).

Pad experiments

Agarose pads were prepared by melting medium supplemented with appropriate carbon sources and 1.5% of low-melt agarose. 1 mL of hot mix was placed between two 2 × 2 cm microscope cover slips and let to solidify for one hour in a Petri dish. The upper cover slip was then removed and the pad was cut into four distinct pieces to accommodate multiple strains. Overnight cultures of the reporter strain and the wild-type strain were diluted to an OD₆₀₀ of 0.1, and 2 μL of each culture was spotted onto a distinct section of the pad. The pad was left

to dry for 15 minutes and a microscope slide was then placed on top of the pad. The pad was sealed using paraffin and transferred to the microscope. The same image acquisition setup and parameters were used as described for the mother machine experiments.

In total, two pad experiments were conducted in order to quantify the autofluorescence of our reporter strain as compared to the autofluorescence of the wild-type strain. The obtained images were analyzed in ImageJ and 70 cells were manually segmented using the phase-contrast channel. The fluorescence intensity was then extracted for each segmented cell, fluorescence channel and frame. For each cell, the fluorescence intensities were averaged across all frames to obtain a more robust estimate of the autofluorescence.

Image processing

Pre-processing and segmentation. For image pre-processing and segmentation, we used the mother machine segmentation software tool BACMMAN³⁸. Raw images were sorted and imported into the software. After a pre-processing step in which the images were stabilized and de-noised, the microchannels and individual bacteria were segmented on the green fluorescence channel. For each experiment, empty microchannels and microchannels presenting double-loading were discarded from the analysis, along with a few cells that stopped growing at various phases of the experiment. The segmentation was performed using the BacteriaFluo algorithm. In our study, we included around 350 mother cells (Table S2). After segmentation, the mother cells and first-generation daughters were visually checked and the few segmentation errors (<5%) manually corrected.

Post-processing. For each segmented cell, we obtained the mean fluorescence intensity [RFU/ pixel], averaged over all pixels belonging to the segmented cell area, the length of each cell [pixel] and various other statistics containing information on position and lineage. For the chosen settings, one pixel corresponds to 0.11 μm . These results were imported into Python where several post-processing steps were carried out. The camera noise and background were corrected for each channel by subtracting the base value we obtained with a closed shutter.

The autofluorescence was evaluated using pad experiments, as described above. The autofluorescence of the wild-type strain was found to be around zero, after background correction, and negligible in comparison with the fluorescence emitted by the reporter strains (Fig. S20). We therefore applied no autofluorescence correction to the measured fluorescence intensities.

To detect any reporter photobleaching effects in our experiments, we performed a microfluidics control experiment with the reporter strain growing in balanced growth in minimal medium with acetate (Table S2). The same image acquisition parameters as described above for the microfluidics experiments were used. The images thus obtained were segmented and the fluorescence intensity extracted (Fig. S21). The curve was fitted by a straight line and the obtained slope coefficient was found to be indistinguishable from zero, so no photobleaching correction was applied in the measurement model.

Model definition and calibration

To reconstruct the ribosome synthesis rates from single-cell fluorescence data, we developed a mechanistic model that takes into account fluorescent protein maturation, degradation and growth dilution.

GFP has first-order maturation kinetics¹⁰³, so the dynamics of the RpsB-GFPmut2 fusion in the Rib strain can be described by the following simple model (Supplementary Note 1 and⁴⁰):

$$\frac{d}{dt}r_{im}(t) = v_r(t) - (\mu(t) + \gamma + k_{mat})r_{im}(t), \quad (5)$$

$$\frac{d}{dt}r_m(t) = k_{mat}r_{im}(t) - (\mu(t) + \gamma)r_m(t). \quad (6)$$

r_{im} and r_m refer to the concentrations of ribosomes tagged with immature and mature GFP, respectively, in units RFU/pixel. Maturation is characterized by the constant k_{mat} [1/h]. Protein degradation is determined by the degradation constant γ [1/h]. $v_r(t)$ is the time-varying synthesis rate of ribosomal proteins, or ribosome synthesis rate for short, that can be reconstructed from single-cell fluorescence data using the methods described below. Note that the sum of Eqs 5 and 6 results in Eq. 1 in the main text, describing the dynamics of the total (mature and immature) ribosome concentration. Table S4 lists the symbols used in the model.

The maturation and degradation parameters for the GFPmut2 reporter were determined experimentally in previous work⁴⁰, in experiments where an antibiotic (Chloramphenicol) was added to a growing culture to stop translation and the subsequent decrease in fluorescence was measured. The parameter values are summarized in Table S3.

Growth-rate estimation

Growth rates of mother cells over the entire duration of an experiment were inferred from measured cell lengths by means of a custom-made estimation method. The method is based on the following model of growth rate $\mu(t)$:

$$\frac{d}{dt}L(t) = \mu(t)L(t), \quad (7)$$

where $L(t)$ is the time-varying length of a mother cell, expressed in pixel units. Cell length is a good approximation of cell size in rod-shaped bacteria like *E. coli*^{2,37}. Like in other recent studies^{41–44}, we did not assume that growth rates are constant between two consecutive cell divisions. However, growth rates were assumed constant between two consecutive measurement times, which is reasonable given the sampling density (once every 11–13 min, corresponding to 4–30 length measurements per generation).

As explained in Supplementary Note 2, the above assumptions result in an estimation problem defined for a piecewise-linear model with as many equations as cell length measurements. Because the solutions of this problem are underdetermined by the (noisy) experimental data, we employed a regularized least squares method¹⁰⁴. Regularization involves a cost function penalizing rapid changes in growth rate, multiplied with a regularization parameter $\lambda > 0$. We fixed an appropriate value for λ by means of cross-validation¹⁰⁵. In particular, we estimated an optimal value $\hat{\lambda}^c$ for every mother cell c considered in an experiment. The median of these estimates was used as our best choice for λ , which makes the latter robust to measurement outliers caused by a variety of experimental errors, such as an occasional loss of focus. In order to allow for rapid changes in growth rate after nutrient upshifts and downshifts, no regularization was enforced immediately after a growth transition (Supplementary Note 2). All of the above-mentioned computations were carried out in Python 3.6, using the code available at <https://gitlab.inria.fr/microcosme/estimationcodemicrofluidicsdata> and in a dedicated Code Ocean capsule (<https://doi.org/10.24433/CO.6310888>).

The results of the growth-rate estimation method were validated in two different ways. First, we assessed the performance of the method by applying it to synthetic cell length data generated by means of Eq. (7) for a given time-course growth-rate profile. To the cell lengths thus generated, we added Gaussian noise in agreement with the experimentally observed distribution. From these synthetic data, the method succeeded in robustly reconstructing the known growth-rate profile (Fig. S22). Second, we compared the performance of the method with a baseline approach consisting in the fit of a linear curve to log-transformed length data between two consecutive cell divisions, corresponding to the assumption of a constant growth rate during each generation time. During balanced growth, when the growth rate is

approximately constant, the two methods give comparable results. However, when the assumption is not satisfied, especially during transitions between growth phases, our method gives more plausible estimates (Fig. S7).

Inference of ribosome synthesis rates

Kalman smoothing method. For each mother cell, the unknown ribosome synthesis rate $\nu_r(t)$ was inferred from noisy fluorescence intensity measurements $y_k = r_m(t) + \epsilon_k$, obtained at time-points t_k , $k = 1, \dots, n$. The measurement errors ϵ_k form a sequence of independent random variables with mean zero and variance s_k^2 . We assumed that all measurements obtained in a specific growth phase in an experiment, that is, in a specific growth medium, have the same variance. The variance was estimated from the fluorescence data when the cells had been in balanced growth in the medium for more than 6 generations, and $\nu_r(t)$ can be assumed time-invariant. In particular, we determined the variance from the observed standard deviation around a constant mean in the corresponding time interval. In order to increase the robustness of the estimate, we selected the median of the values for all individual mother cells.

Estimation of the unknown synthesis rate profile demands the formulation of a probabilistic prior on $\nu_r(t)$. This prior was expressed in the form of a stochastic differential equation

$$d\nu_r(t) = -\theta \cdot \nu_r(t) \cdot dt + \sigma \cdot dW(t), \tag{8}$$

where $W(t)$ is the standard Wiener (white noise) process, and $\sigma, \theta > 0$ are parameters defining the (magnitude and time-scale of) fluctuations in the ribosome synthesis rate⁴⁰. We assume that $\nu_r(0)$ has a zero-mean Gaussian distribution with variance $\sigma^2/(2\theta)$, which implies that the process is stationary. The parameters σ and θ play the role of regularization parameters, ensuring that the inference of $\nu_r(t)$ is robust to measurement noise. We denote the optimal values for these parameters by $\hat{\sigma}$ and $\hat{\theta}$ (see below).

With Eq. (8), the problem of calculating an optimal estimate $\hat{\nu}_r(t)$ for $\nu_r(t)$, given fluorescence intensity measurements y_1, \dots, y_n , becomes the Bayesian problem of calculating the conditional expectation

$$\hat{\nu}_r(t) = \mathbb{E}[\nu_r(t) | y_1, \dots, y_n]. \tag{9}$$

This reconstruction is optimal in the sense that it minimizes the variance of the estimation error at any time t ¹⁰⁶. In order to solve the above problem, the measurement model and the stochastic prior were combined with the maturation model of the green reporter protein (Eqs. (5), (6)), giving rise to the following linear stochastic differential equation model:

$$\begin{aligned} d \begin{bmatrix} \mathbf{x}(t) \\ \nu_r(t) \end{bmatrix} &= \begin{bmatrix} \mathbf{F}(t) & \mathbf{G}(t) \\ 0 & -\hat{\theta} \end{bmatrix} \begin{bmatrix} \mathbf{x}(t) \\ \nu_r(t) \end{bmatrix} dt + \begin{bmatrix} 0 \\ \hat{\sigma} \end{bmatrix} dW(t), \\ y_k &= \begin{bmatrix} \mathbf{C} & 0 \end{bmatrix} \begin{bmatrix} \mathbf{x}(t_k) \\ \nu_r(t_k) \end{bmatrix} + \epsilon_k. \end{aligned} \tag{10}$$

The vector \mathbf{x} represents the state of the system, equal to $[r_{im}, r_m]$. Matrices $\mathbf{F}(t)$ and $\mathbf{G}(t)$ depend on the kinetic parameters in the maturation model, whose values are known (Table S3), as well as the estimated growth-rate profile $\hat{\mu}(t)$, which was derived as explained above. More precisely, we have

$$\begin{aligned} \mathbf{F}(t) &= \begin{bmatrix} -(\hat{\mu}(t) + \gamma + k_{mat}) & 0 \\ k_{mat} & -(\hat{\mu}(t) + \gamma) \end{bmatrix}, \\ \mathbf{G}(t) &= \begin{bmatrix} 1 \\ 0 \end{bmatrix}, \quad \mathbf{C} = \begin{bmatrix} 0 \\ 1 \end{bmatrix}. \end{aligned} \tag{11}$$

Recasting the system in the above form allowed the use of standard Kalman filtering and smoothing methods⁶⁹ to compute $\hat{\nu}_r(t)$ from

the fluorescence intensity measurements. Supplementary Note 2 explains how Kalman filtering and smoothing were instantiated for this specific problem. Instead of solving the estimation problem for the entire measurement time-series, we treated the growth phases in different media separately, like for growth-rate estimation. At the medium switching times separating the growth phases, the ribosome synthesis rate is expected to rapidly change over a short time interval, so that a smooth reconstruction of $\nu_r(t)$ would be artificial. Note that the method also returns an estimate of the time-varying state of the system, that is, $[\hat{r}_{im}(t), \hat{r}_m(t)]$. This output is used to estimate the total ribosome concentration $\hat{r}(t) = \hat{r}_{im}(t) + \hat{r}_m(t)$, taking into account both the observed and non-observed ribosomes.

The computational complexity of the whole procedure is linear in the number of data points n , and is mostly determined by the inversion of the (small) matrices in Eq. (10). For a single mother cell with fluorescence time-series of $n = 300$ points (our case), the Python implementation using function `odeint` of the `scipy.integrate` module for numerical integration, requires around 3 seconds. If the Gaussian assumptions are violated, the estimates computed by this procedure have the interpretation of optimal estimates (minimal error variance) in the class of linear functions of the data¹⁰⁶. Thanks to this, the method is robust to moderate deviations from Gaussianity.

Automatic tuning of regularization parameters. An optimal choice of σ and θ was determined by solving the maximum likelihood problem

$$(\hat{\theta}, \hat{\sigma}) = \arg \max_{(\theta, \sigma)} f_{\theta, \sigma}(y_1, \dots, y_n), \tag{12}$$

for every mother cell in the dataset, where $f_{\theta, \sigma}(\cdot)$ is the probability density function for the observed data of a given mother cell under the stochastic prior of Eq. (8)⁴⁰. In practice, for any value of (θ, σ) , evaluation of the above likelihood can be performed by Kalman filtering, in a similar way as for the estimation problem above. The details are given in Supplementary Note 2.

The computational efficiency of Kalman filtering is important for the automatic tuning of the regularization parameters, because the optimization problem requires a large number of evaluations of the right-hand side of Eq. (12). Optimization was carried out numerically by the Python function `minimize` of `scipy.optimize`. In a typical experiment with 100 mother cells and $n = 300$, the total computation time of the tuning procedure was around 2 hours.

For every mother cell c , we computed optimal regularization parameters $(\hat{\theta}^c, \hat{\sigma}^c)$ in the way described above. The final choice of the regularization parameters consisted in choosing the median of the values over all c . The latter value was then used for the estimation of the ribosome synthesis rate from the time-series data for every individual mother cell.

Validation of the method. The method was validated in two different ways. First, we generated synthetic fluorescence data using the model of Eq. (10), for a given ribosome synthesis rate profile and noise characteristics corresponding to those of the real data. The Kalman smoothing estimation method was able to accurately reconstruct $\nu_r(t)$ (Fig. S23). Second, we visually inspected the fit of the fluorescence intensities predicted by the model along with the inferred ribosome synthesis rate and the actually observed fluorescence intensities for a large number of cells (Fig. 1). This was done both for the chosen optimal regularization parameters and (as a sensitivity test) for discarded non-optimal choices.

Clustering of resource allocation strategies

In order to visualize shared adaptation patterns across individual cells considered in an experiment, we clustered the reconstructed ribosome synthesis rates after an upshift from acetate to glucose by means of a k-means clustering algorithm¹⁰⁷ implemented in Python (`sklearn`

package¹⁰⁸). Since all cells reach approximately the same steady-state levels of $\nu_r(t)$, we only clustered the data during the first two hours after the upshift (Fig. S12). Before we checked that the mother cells in the clusters are homogeneously distributed over the positions in the microfluidics device.

Predictions of dynamic growth laws

We experimentally tested the predictions of the jump in growth rate directly after the acetate-glucose upshift in the reference experiment, using the theoretical models of Mori et al.²⁵ and Korem Kohanin et al.²⁶.

Let $\tilde{\mu}_0 = \mu_0/\mu_{max}$ be the growth rate on acetate before the upshift (μ_0), normalized with respect to the maximum growth rate of the *E. coli* BW25113 strain (μ_{max}). Similarly, $\tilde{\mu}_1 = \mu_1/\mu_{max}$ and $\tilde{\mu}_{glc} = \mu_{glc}/\mu_{max}$ are the normalized growth rate directly after the upshift and the normalized growth rate on glucose that is eventually reached after the upshift, respectively. We used the following model (Eq. 7 in ref. 26):

$$\tilde{\mu}_1 = \sqrt{\tilde{\mu}_0 \tilde{\mu}_{glc}} \frac{1 - \tilde{\mu}_0}{\tilde{\mu}_0 - 2\tilde{\mu}_0 \tilde{\mu}_{glc} + \tilde{\mu}_{glc}}, \quad (13)$$

to predict $\tilde{\mu}_1$ from values for μ_0 and μ_{glc} from our data and a value for μ_{max} from the literature. In particular, we computed μ_0 as the average value of the growth rate on acetate during 4 h preceding the upshift. Idem for μ_{glc} , averaged over 2 h more than 10 generations after the upshift. For μ_{max} , we used the value 1.6 h^{-1} for growth of the BW25113 strain in LB medium¹⁰⁹. The experimental values for $\tilde{\mu}_1$ were obtained by dividing the growth rate directly after the upshift by the value of μ_{max} . The model was applied both for values obtained for each individual mother cell and for values averaged over all mother cells in the experiment.

Let ϕ_0 and ϕ_{glc} be the ribosomal protein fractions during balanced growth on acetate before the upshift and during balanced growth on glucose after the upshift, respectively. The following model (Eq. 8 in ref. 25) predicts the growth rate directly after the upshift:

$$\mu_1 = \mu_0 \frac{\phi_0}{\phi_{glc}} = \mu_0 \frac{r_0}{r_{glc}}, \quad (14)$$

where we have replaced the ratio of ribosomal protein fractions ϕ_0/ϕ_{glc} by the ratio of ribosome concentrations r_0/r_{glc} during balanced growth on acetate before the upshift and on glucose after the upshift. If the total protein concentration remains approximately constant between these two time-points, then the two ratios are equivalent. We computed r_0 and r_{glc} from the fluorescence data, by averaging the total ribosome concentration returned by the inference algorithm in the same time-intervals as μ_0 and μ_{glc} above. Combined with the growth rate μ_0 , computed as above, this yields a predicted value for μ_1 . This prediction was compared with the experimentally determined value for μ_1 . Like for the previous model, the comparison was carried out for the values obtained for each individual mother cell and the average value over all mother cells in the experiment.

Reporting summary

Further information on research design is available in the Nature Portfolio Reporting Summary linked to this article.

Data availability

All data supporting the findings of this study are available within the paper and its Supplementary Information. Source data are provided with this paper.

Code availability

The Python code to generate the figures in the main text and the Supplementary Information from the data are available as <https://gitlab.inria.fr/microcosme/estimationcodemicrofluidicsdata> and the dedicated Code Ocean capsule (<https://doi.org/10.24433/CO.6310888>).

References

- Hwa, T. & Scott, M. Bacterial growth laws and their applications. *Curr. Opin. Biotechnol.* **22**, 559–565 (2011).
- Jun, S., Si, F., Pugatch, R. & Scott, M. Fundamental principles in bacterial physiology - history, recent progress, and the future with focus on cell size control: A review. *Rep. Prog. Phys.* **81**, 056601 (2018).
- Bruggeman, F. J., Planqué, R., Molenaar, D. & Teusink, B. Searching for principles of microbial physiology. *FEMS Microbiol. Rev.* **44**, 821–844 (2020).
- Schaechter, M., Maaløe, O. & Kjeldgaard, O. N. Dependency on medium and temperature of cell size and chemical composition during balanced growth of *Salmonella typhimurium*. *J. Gen. Microbiol.* **19**, 592–606 (1958).
- Neidhardt, F. C. & Magasanik, B. Studies on the role of ribonucleic acid in the growth of bacteria. *Biochim. Biophys. Acta* **42**, 99–116 (1960).
- Forchhammer, J. & Lindahl, L. Growth rate of polypeptide chains as a function of the cell growth rate in a mutant of *Escherichia coli* 15. *J. Mol. Biol.* **55**, 563–568 (1971).
- Alberghina, F. A., Sturani, E. & Gohlke, R. J. Levels and rates of synthesis of ribosomal ribonucleic acid, transfer ribonucleic acid, and protein in *Neurospora crassa* in different steady states of growth. *J. Biol. Chem.* **250**, 4381–4388 (1975).
- Bremer, H. & Dennis, P. P. Modulation of chemical composition and other parameters of the cell at different exponential growth rates. *EcoSal Plus* **3**, 1–48 (2008).
- Scott, M., Gunderson, W. C., Mateescu, M. E., Zhang, Z. & Hwa, T. Interdependence of cell growth and gene expression: origins and consequences. *Science* **330**, 1099–1102 (2010).
- Metzl-Raz, E. et al. Principles of cellular resource allocation revealed by condition-dependent proteome profiling. *eLife* **6**, e28034 (2017).
- Zavřel, T. et al. Quantitative insights into the cyanobacterial cell economy. *eLife* **8**, e42508 (2019).
- Schmidt, A. et al. The quantitative and condition-dependent *Escherichia coli* proteome. *Nat. Biotechnol.* **34**, 104–110 (2016).
- Hui, S. et al. Quantitative proteomic analysis reveals a simple strategy of global resource allocation in bacteria. *Mol. Syst. Biol.* **11**, 784 (2015).
- Mairet, F., Gouzé, J.-L. & de Jong, H. Optimal proteome allocation and the temperature dependence of microbial growth laws. *npj Syst. Biol. Appl.* **7**, 1–11 (2021).
- Molenaar, D., van Berlo, R., de Ridder, D. & Teusink, B. Shifts in growth strategies reflect tradeoffs in cellular economics. *Mol. Syst. Biol.* **5**, 323 (2009).
- Scott, M., Klumpp, S., Mateescu, M. E. & Hwa, T. Emergence of robust growth laws from optimal regulation of ribosome synthesis. *Mol. Syst. Biol.* **10**, 747 (2014).
- Weiß, A. Y., Oyarzún, D. A., Danos, V. & Swain, S. P. Mechanistic links between cellular trade-offs, gene expression, and growth. *Proc. Natl Acad. Sci. USA* **112**, E1038–E1047 (2015).
- Giordano, N., Mairet, F., Gouzé, J.-L., Geiselman, J. & de Jong, H. Dynamical allocation of cellular resources as an optimal control problem: Novel insights into microbial growth strategies. *PLoS Comput. Biol.* **12**, e1004802 (2016).
- Bosdriesz, E., Molenaar, D., Teusink, B. & Bruggeman, J. F. How fast-growing bacteria robustly tune their ribosome concentration to approximate growth-rate maximization. *FEBS J.* **282**, 2029–2044 (2015).

20. Hu, X.-P., Dourado, H., Schubert, P. & Lercher, J. M. The protein translation machinery is expressed for maximal efficiency in *Escherichia coli*. *Nat. Commun.* **11**, 5260 (2020).
21. Zaslaver, A. et al. Invariant distribution of promoter activities in *Escherichia coli*. *PLoS Comput. Biol.* **5**, e1000545 (2009).
22. Blount, Z. D. The unexhausted potential of *E. coli*. *eLife* **4**, e05826 (2015).
23. Erickson, D. W. et al. A global resource allocation strategy governs growth transition kinetics of *Escherichia coli*. *Nature* **551**, 119–123 (2017).
24. Bremer, H. & Dennis, P. P. Transition period following a nutritional shift-up in the bacterium *Escherichia coli* B/r: stable RNA and protein synthesis. *J. Theor. Biol.* **52**, 365–382 (1975).
25. Mori, M., Schink, S., Erickson, W. D., Gerland, U. & Hwa, T. Quantifying the benefit of a proteome reserve in fluctuating environments. *Nat. Commun.* **8**, 1225 (2017).
26. Korem Kohanim, Y. et al. A bacterial growth law out of steady state. *Cell Rep.* **23**, 2891–2900 (2018).
27. Balaban, N. Q., Merrin, J., Chait, R., Kowalik, L. & Leibler, S. Bacterial persistence as a phenotypic switch. *Science* **305**, 1622–1625 (2004).
28. Süel, G., Garcia-Ojalvo, J., Liberman, L. & Elowitz, M. An excitable gene regulatory circuit induces transient cellular differentiation. *Nature* **440**, 545–550 (2006).
29. Ferrezuelo, F. et al. The critical size is set at a single-cell level by growth rate to attain homeostasis and adaptation. *Nat. Commun.* **3**, 1012 (2012).
30. Wakamoto, Y. et al. Dynamic persistence of antibiotic-stressed mycobacteria. *Science* **339**, 91–95 (2013).
31. Solopova, A. et al. Bet-hedging during bacterial diauxic shift. *Proc. Natl Acad. Sci. USA* **111**, 7427–7432 (2014).
32. Taheri-Araghi, S. et al. Cell-size control and homeostasis in bacteria. *Curr. Biol.* **25**, 385–391 (2015).
33. Bamford, R. A. et al. Investigating the physiology of viable but non-culturable bacteria by microfluidics and time-lapse microscopy. *BMC Biol.* **15**, 121 (2017).
34. Koch, A. L. & Deppe, S. C. In vivo assay of protein synthesizing capacity of *Escherichia coli* from slowly growing chemostat cultures. *J. Mol. Biol.* **55**, 549–562 (1971).
35. Bakshi, S., Siryaporn, A., Goulian, M. & Weisshaar, C. J. Super-resolution imaging of ribosomes and RNA polymerase in live *Escherichia coli* cells. *Mol. Microbiol.* **85**, 21–38 (2012).
36. Baba, T., Wanner, L. B. & Mori, H. Construction of *Escherichia coli* K-12 in-frame, single-gene knockout mutants: the Keio collection. *Mol. Syst. Biol.* **2**, 2006–2008 (2006).
37. Wang, P. et al. Robust growth of *Escherichia coli*. *Curr. Biol.* **20**, 1099–1103 (2010).
38. Ollion, J., Elez, M. & Robert, L. High-throughput detection and tracking of cells and intracellular spots in mother machine experiments. *Nat. Protoc.* **14**, 3144–3161 (2019).
39. Basan, M. et al. A universal tradeoff between growth and lag in fluctuating environments. *Nature* **584**, 470–474 (2020).
40. Pavlou, A., Cinquemani, E., Geiselmann, J. & de Jong, H. Maturation models are necessary to obtain unbiased estimates of promoter activity. *Biophys. J.* **121**, 4179–4188 (2022).
41. Cylke, A. & Banerjee, S. Super-exponential growth and stochastic size dynamics in rod-like bacteria. *Biophys. J.* **122**, 1254–1267 (2023).
42. Kiviet, D. et al. Stochasticity of metabolism and growth at the single-cell level. *Nature* **514**, 376–379 (2014).
43. Nordholt, N., van Heerden, J. & Bruggeman, F. Biphasic cell-size and growth-rate homeostasis by single *Bacillus subtilis* cells. *Curr. Biol.* **30**, 2238–2247 (2020).
44. Nguyen, J. et al. A distinct growth physiology enhances bacterial growth under rapid nutrient fluctuations. *Nat. Commun.* **12**, 3662 (2021).
45. Pinhal, S., Ropers, D., Geiselmann, J. & de Jong, H. Acetate metabolism and the inhibition of bacterial growth by acetate. *J. Bacteriol.* **201**, e00147–19 (2019).
46. Gerosa, L., Kochanowski, K., Heinemann, M. & Sauer, U. Dissecting specific and global transcriptional regulation of bacterial gene expression. *Mol. Syst. Biol.* **9**, 658 (2013).
47. Kailath, T. Linear estimation. *IEEE Trans. Inf. Theory* **51**, 2236–2240 (2005).
48. Valgepea, K., Adamberg, K., Seiman, A. & Vilu, R. *Escherichia coli* achieves faster growth by increasing catalytic and translation rates of proteins. *Mol. Biosyst.* **9**, 2344–2358 (2013).
49. Sanders, S., Joshi, K., Levin, P. & Iyer-Biswas, S. Beyond the average: An updated framework for understanding the relationship between cell growth, DNA replication, and division in a bacterial system. *PLoS Genet.* **19**, e1010505 (2023).
50. Ehrenberg, M., Bremer, H. & Dennis, P. Medium-dependent control of the bacterial growth rate. *Biochimie* **95**, 643–658 (2013).
51. Young, R. & Bremer, H. Polypeptide-chain-elongation rate in *Escherichia coli* B/r as a function of growth rate. *Biochem. J.* **160**, 185–194 (1976).
52. Woldringh, C. & Binnerts, A. M. J. S. Variation in *Escherichia coli* buoyant density measured in Percoll gradients. *J. Bacteriol.* **148**, 58–63 (1981).
53. Kubitschek, H., Baldwin, W., Schroeter, S. & Graetzer, R. Independence of buoyant cell density and growth rate in *Escherichia coli*. *J. Bacteriol.* **158**, 296–299 (1984).
54. Pedersen, S. *Escherichia coli* ribosomes translate in vivo with variable rate. *EMBO J.* **3**, 2895–2898 (1984).
55. Bremer, H. & Dennis, P. Modulation of chemical composition and other parameters of the cell by growth rate. In Neidhardt, F. et al. editors, *Escherichia coli and Salmonella: Cellular and Molecular Biology*, ASM Press, Washington, DC, 1553–1569. 2nd edition (1996).
56. Basan, M. et al. Inflating bacterial cells by increased protein synthesis. *Mol. Syst. Biol.* **11**, 836 (2015).
57. Dai, X. et al. Reduction of translating ribosomes enables *Escherichia coli* to maintain elongation rates during slow growth. *Nat. Microbiol.* **2**, 1–9 (2016).
58. Li, S.-J. et al. *Escherichia coli* translation strategies differ across carbon, nitrogen and phosphorus limitation conditions. *Nat. Microbiol.* **3**, 939–947 (2018).
59. van den Berg, H. A., Kiselev, N. Y., A, S. L. M. Kooijman & Orlov, V. M. Optimal allocation between nutrient uptake and growth in a microbial trichome. *J. Math. Biol.* **37**, 28–48 (1998).
60. Zaslaver, A. et al. A comprehensive library of fluorescent transcriptional reporters for *Escherichia coli*. *Nat. Methods* **3**, 623–628 (2006).
61. O'Brien, E., Utrilla, J. & Palsson, B. Quantification and classification of *E. coli* proteome utilization and unused protein costs across environments. *PLoS Comput. Biol.* **12**, e1004998 (2016).
62. Biselli, E., Schink, J. S. & Gerland, U. Slower growth of *Escherichia coli* leads to longer survival in carbon starvation due to a decrease in the maintenance rate. *Mol. Syst. Biol.* **16**, e9478 (2020).
63. Balakrishnan, R., de Silva, R. T., Hwa, T. & Cremer, J. Suboptimal resource allocation in changing environments constrains response and growth in bacteria. *Mol. Syst. Biol.* **17**, e10597 (2021).
64. Schuetz, R., Zamboni, N., Zampieri, M., Heinemann, M. & Sauer, U. Multidimensional optimality of microbial metabolism. *Science* **336**, 601–604 (2012).
65. Kjeldgaard, N. O., Maaløe, O. & Schaechter, M. The transition between different physiological states during balanced growth of *Salmonella typhimurium*. *J. Gen. Microbiol.* **19**, 607–16 (1958).
66. Dennis, P. Synthesis of individual ribosomal proteins in *Escherichia coli* B/r. *J. Mol. Biol.* **89**, 223–232 (1974).

67. Koch, A. The inefficiency of ribosomes functioning in *Escherichia coli* growing at moderate rates. *J. Gen. Microbiol.* **116**, 165–171 (1980).
68. Brunschede, H., Dove, T. & Bremer, H. Establishment of exponential growth after a nutritional shift-up in *Escherichia coli* B/r: accumulation of deoxyribonucleic acid, ribonucleic acid, and protein. *J. Bacteriol.* **129**, 1020–1033 (1977).
69. De Nicolao, G. & Ferrari-Trecate, G. Regularization networks for inverse problems: A state-space approach. *Automatica* **39**, 669–676 (2003).
70. Zulkower, V., Page, M., Ropers, D., Geiselman, J. & de Jong, H. Robust reconstruction of gene expression profiles from reporter gene data using linear inversion. *Bioinformatics* **31**, i71–i79 (2015).
71. Maaløe, O. Regulation of the protein-synthesizing machinery – Ribosomes, tRNA, factors, and so on. In *Biological Regulation and Development* (ed. Goldberger, R.) 487–542 (Springer, Boston, MA, 1979).
72. Odermatt, P. et al. Variations of intracellular density during the cell cycle arise from tip-growth regulation in fission yeast. *eLife* **10**, e64901 (2021).
73. Oldewurtel, E., Kitahara, Y. & van Teeffelen, S. Robust surface-to-mass coupling and turgor-dependent cell width determine bacterial dry-mass density. *Proc. Natl Acad. Sci. USA* **118**, e2021416118 (2021).
74. Nemati, S. et al. Density fluctuations, homeostasis, and reproduction effects in bacteria. *Commun. Biol.* **5**, 397 (2022).
75. Taniguchi, Y. et al. Quantifying *E. coli* proteome and transcriptome with single-molecule sensitivity in single cells. *Science* **329**, 533–539 (2010).
76. Afroz, T., Biliouris, K., Kaznessis, Y. & Beisel, C. Bacterial sugar utilization gives rise to distinct single-cell behaviours. *Mol. Microbiol.* **93**, 1093–1103 (2014).
77. Fritz, G. et al. Single cell kinetics of phenotypic switching in the arabinose utilization system of *E. coli*. *PLoS One* **9**, e89532 (2014).
78. Keren, L. et al. Noise in gene expression is coupled to growth rate. *Genome Res.* **25**, 1893–1902 (2015).
79. Sampaio, N., Blassick, C., Andreani, V., Lugagne, J. & Dunlop, M. Dynamic gene expression and growth underlie cell-to-cell heterogeneity in *Escherichia coli* stress response. *Proc. Natl Acad. Sci. USA* **119**, e2115032119 (2022).
80. Brettner, L. & Geiler-Samerotte, K. Single-cell heterogeneity and the growth laws. *BioRxiv* preprint: <https://doi.org/10.1101/2024.04.19.590370> (2024).
81. Thomas, P., Terradot, G., Danos, V. & Weiße, A. Y. Sources, propagation and consequences of stochasticity in cellular growth. *Nat. Commun.* **9**, 4528 (2018).
82. Nozoe, T., Kussell, E. & Wakamoto, Y. Inferring fitness landscapes and selection on phenotypic states from single-cell genealogical data. *PLoS Genet.* **13**, e1006653 (2017).
83. Susman, L. et al. Individuality and slow dynamics in bacterial growth homeostasis. *Proc. Natl Acad. Sci. USA* **115**, E5679–87 (2018).
84. Tanouchi, Y. et al. A noisy linear map underlies oscillations in cell size and gene expression in bacteria. *Nature* **523**, 357–360 (2015).
85. Elowitz, M., Levine, A., Siggia, E. & Swain, P. Stochastic gene expression in a single cell. *Science* **297**, 1183–1186 (2002).
86. Raser, J. & O’Shea, E. Noise in gene expression: origins, consequences, and control. *Science* **309**, 62010–62013 (2005).
87. Bruggeman, F. & Teusink, B. Living with noise: on the propagation of noise from molecules to phenotype and fitness. *Curr. Opin. Syst. Biol.* **8**, 144–150 (2018).
88. Cashel, M. & Gallant, J. Two compounds implicated in the function of the RC gene of *Escherichia coli*. *Nature* **221**, 838–841 (1969).
89. Potrykus, K., Murphy, H., Philippe, N. & Cashel, M. ppGpp is the major source of growth rate control in *E. coli*. *Environ. Microbiol.* **13**, 563–575 (2011).
90. Hauryliuk, V., Atkinson, C. G., Murakami, S. K., Tenson, T. & Gerdes, K. Recent functional insights into the role of (p)ppGpp in bacterial physiology. *Nat. Rev. Microbiol.* **13**, 298–309 (2015).
91. Irving, S. E., Choudhury, R. N. & Corrigan, M. R. The stringent response and physiological roles of (pp)pGpp in bacteria. *Nat. Rev. Microbiol.* **19**, 256–271 (2021).
92. Wu, C. et al. Cellular perception of growth rate and the mechanistic origin of bacterial growth law. *Proc. Natl Acad. Sci. USA* **119**, e2201585119 (2022).
93. Kotte, O., Volkmer, B., Radzikowski, J. & Heinemann, M. Phenotypic bistability in *Escherichia coli*’s central carbon metabolism. *Mol. Syst. Biol.* **10**, 736 (2014).
94. Gausing, K. Regulation of ribosome synthesis in *E. coli*. In *Ribosomes: Structure, Function and Genetics* (eds. Chambliss, G. et al.) 693–718 (University Park Press, Baltimore, 1980).
95. Rao, C., Wolf, D. & Arkin, A. Control, exploitation and tolerance of intracellular noise. *Nature* **420**, 231–237 (2002).
96. Raj, A. & van Oudenaarden, A. Nature, nurture, or chance: Stochastic gene expression and its consequences. *Cell* **135**, 216–226 (2008).
97. Braun, V. FhuA (TonA), the career of a protein. *J. Bacteriol.* **191**, 3431–3436 (2009).
98. Guzman, L. M., Belin, D., Carson, J. M. & Beckwith, J. Tight regulation, modulation, and high-level expression by vectors containing the arabinose PBAD promoter. *J. Bacteriol.* **177**, 4121–4130 (1995).
99. Sharan, S. K., Thomason, C. L., Kuznetsov, G. S. & Court, L. D. Recombineering: a homologous recombination-based method of genetic engineering. *Nat. Protoc.* **4**, 206–223 (2009).
100. Miller, J. H. *Experiments in Molecular Genetics*. (Cold Spring Harbor Laboratory, Cold Spring Harbor, New York, 1972).
101. Martin, Y., Page, M., Blanchet, C. & de Jong, H. WellInverter: a web application for the analysis of fluorescent reporter gene data. *BMC Bioinform.* **20**, 309 (2019).
102. Edelstein, A., Amodaj, N., Hoover, K., Vale, R. & Stuurman, N. Computer control of microscopes using μ Manager. *Curr. Protoc. Mol. Biol.* **92**, 14.20.1–14.20.17 (2010).
103. Balleza, E., Kim, M. J. & Cluzel, P. Systematic characterization of maturation time of fluorescent proteins in living cells. *Nat. Methods* **15**, 47–51 (2018).
104. De Nicolao, G., Sparacino, G. & Cobelli, C. Nonparametric input estimation in physiological systems: Problems, methods, and case studies. *Automatica* **33**, 851–870 (1997).
105. Hastie, T., Tibshirani, R. & Friedman, H. J. *The Elements of Statistical Learning: Data Mining, Inference, and Prediction* (2001). Springer Science & Business Media, New York, NY, 2nd edition.
106. Kailath, T., Sayed, H. A. & Hassibi, B. *Linear Estimation*. Prentice Hall, Upper Saddle River, NJ (2000).
107. Likas, A., Vlassis, N. & Verbeek, J. J. The global k-means clustering algorithm. *Pattern Recognit.* **36**, 451–461 (2003).
108. Buitinck, L. et al. API design for machine learning software: experiences from the scikit-learn project. In *ECML PKDD Workshop: Languages for Data Mining and Machine Learning*, 108–122 (2013).
109. Volkmer, B. & Heinemann, M. Condition-dependent cell volume and concentration of *Escherichia coli* to facilitate data conversion for systems biology modeling. *PLoS ONE* **6**, e23126 (2011).

Acknowledgements

This work was supported by the ANR project Maximic (ANR-17-CE40-0024). The authors would like to thank Grégory Batt and Jean-Luc Gouzé for comments on a previous version of the manuscript.

Author contributions

A.P., J.G., and H.d.J. designed the study. A.P., N.G., and C.P. constructed the strains. A.P. and N.G. determined the experimental conditions. A.P. performed the experiments. I.M. and M.V.M.G. developed, implemented and supervised the fluorescence microscopy experiments in pads and mother machine. A.P., E.C., and H.d.J. developed the mathematical models. A.P. and E.C. developed and implemented the growth-rate and resource allocation inference procedures. A.P., E.C., J.G., and H.d.J. analyzed the data. A.P., E.C., J.G., and H.d.J. wrote the paper.

Competing interests

The authors declare no competing interests.

Additional information

Supplementary information The online version contains supplementary material available at <https://doi.org/10.1038/s41467-024-55394-5>.

Correspondence and requests for materials should be addressed to Johannes Geiselmann or Hidde de Jong.

Peer review information *Nature Communications* thanks Srividya Iyer-Biswas, who co-reviewed with Kunaal Joshi, and the other, anonymous, reviewers for their contribution to the peer review of this work. A peer review file is available.

Reprints and permissions information is available at <http://www.nature.com/reprints>

Publisher's note Springer Nature remains neutral with regard to jurisdictional claims in published maps and institutional affiliations.

Open Access This article is licensed under a Creative Commons Attribution-NonCommercial-NoDerivatives 4.0 International License, which permits any non-commercial use, sharing, distribution and reproduction in any medium or format, as long as you give appropriate credit to the original author(s) and the source, provide a link to the Creative Commons licence, and indicate if you modified the licensed material. You do not have permission under this licence to share adapted material derived from this article or parts of it. The images or other third party material in this article are included in the article's Creative Commons licence, unless indicated otherwise in a credit line to the material. If material is not included in the article's Creative Commons licence and your intended use is not permitted by statutory regulation or exceeds the permitted use, you will need to obtain permission directly from the copyright holder. To view a copy of this licence, visit <http://creativecommons.org/licenses/by-nc-nd/4.0/>.

© The Author(s) 2024